Elastic reflection waveform inversion with petrophysical model constraints

Daniel Rocha & Paul Sava
Center for Wave Phenomena, Colorado School of Mines

ABSTRACT

Elastic wavefield tomography faces challenging pitfalls due to its multiparameter and multicomponent characters, which are absent in the acoustic case. Inter-parameter crosstalk and the absence of petrophysical constraints may cause elastic inversion to fail, delivering unphysical and artifact-contaminated models. In addition, one of the goals of wavefield tomography is to deliver an earth model that generates accurate and high-quality images; however, this might not be the case for conventional data-domain tomography methods that exclude image optimization during inversion. Therefore, we propose to use the elastic reflection waveform inversion (ERWI) methodology, which inverts both for the background velocity model and for the reflectivity image, coupled with a petrophysical constraint term in the objective function. We demonstrate that constraining ERWI is successful in delivering more plausible models with fewer artifacts and that obey the imposed constraints. We alternate between smooth model and reflectivity updates, keeping both data fitting, image focusing and petrophysical constraints consistent with one another in a common objective function. Compared to unconstrained inversion, our numerical examples show less-contaminated models and higher-quality images, as well as improved convergence and accuracy.

Key words: waveform inversion; least-squares migration; multiparameter; multicomponent; elastic tomography; model constraints

1 INTRODUCTION

As the state-of-the-art technology for imaging subsurface structures in complex geological settings, wavefield tomography involves numerical extrapolation of recorded seismic waves to constrain physical properties (e.g., seismic velocity) as solutions to inverse problems. As opposed to ray-based methods (Bishop et al., 1985; Bording et al., 1987; Lines, 1991; Cerveny, 2005), wavefield tomography is preferred as the main method for high-resolution velocity estimation since it exploits the full waveform and bandwidth of seismic signals in the velocity update, and handles accurate wave propagation in complex media subject to multipathing. Its implementations are generally classified as either data-domain (Lailly, 1983; Tarantola, 1984; Gauthier et al., 1986) and/or as image-domain (Symes and Carazzone, 1991; Sava and Biondi, 2004a; Albertin et al., 2005; Symes, 2008; Yang and Sava, 2011; Diaz et al., 2013; Yang and Sava, 2015).

Full waveform inversion (FWI) (Sirgue et al., 2004; Vigh and Starr, 2008; Virieux and Operto, 2009; Plessix et al., 2013) is the most common data-domain wavefield tomography method, using wavefield extrapolation to obtain a physical model update. Such update is driven by an objective function whose gradient is obtained by crosscorrelation between the state and the adjoint wavefields (Tarantola, 1984; Hindlet and Kolb, 1988; Plessix, 2006). This crosscorrelation between extrapolated wavefields is analogous to imaging conditions in reverse time migration (RTM) (Baysal et al., 1983; McMechan, 1983; Whitmore, 1983). The adjoint wavefield is extrapolated from a data residual, often defined as the difference between observed and modeled data, although the residual could also utilize other discrepancy metric between datasets (Shin and Ha, 2008; Brossier et al., 2010; Ma and Hale, 2013; Chi et al., 2014; Gao et al., 2014; Yang et al., 2018). For image-domain methods, wave-equation migration velocity analysis (WEMVA) (Sava and Biondi, 2004a,b; Shen et al., 2005; Hou and Symes, 2018) stands as the main method that relies on the semblance principle, i.e., the imaged events must be focused if extrapolated with the correct velocity (Symes and Carazzone, 1991; Mulder and ten Kroode, 2002; Shen and Symes, 2008). In this case, the objective function and the associated residual are constructed with extended image gathers; which can be functions of offset, reflection angle or wavefield correlation spatial/temporal lags (Rickett and Sava, 2002; Sava and

Biondi, 2004a; Sava and Vasconcelos, 2011; Yang and Sava, 2011).

Each domain of inversion investigation offers its own benefits and disadvantages. For an initial earth model far from the true one, FWI suffers from cycle skipping, i.e., when the modeled waveforms differ from the observed ones by more than a half cycle. Although FWI is more suitable for diving and direct waves, reflections usually dominate the surface-recorded data and represent the main constituent of migrated images. Conventional FWI does not explicitly constrain the migrated images, possibly delivering models that do not substantially improve image quality. Alternatively, WEMVA seeks the model that delivers the most focused image; however, the obtained model exhibits low resolution and might not directly match observed data, since this optimization is implemented in the image domain.

Reflection waveform inversion (RWI) has recently gained interest as a technology using both reflections in data-domain wavefield tomography and also jointly inverting for the migrated image; (Hicks and Pratt, 2001; Xu et al., 2012; Wang et al., 2013; Guo and Alkhalifah, 2017). This technique exploits an objective function and its residual in the data domain, and separately updates the smooth and rough (i.e., image) parts of the earth model. Least-squares migration robustly computes the rough model (Alves and Biondi, 2016; Feng and Schuster, 2017; Duan et al., 2017; Ren et al., 2017), while optimization via adjoint-state method provides the smooth updates (Tarantola, 1988; Sava, 2014). Therefore, we can classify RWI as a mixed-domain (both data- and image-domain) wavefield tomography method. RWI provides low-wavenumber updates for the smooth earth model, and therefore, avoids high-wavenumber content that harms the inversion at initial iterations.

For any of the aforementioned wavefield tomography methods, one can pursue a multiparameter earth model through elastic wavefield extrapolation (Chang and McMechan, 1987; Yan and Sava, 2011; Ravasi and Curtis, 2013; Duan and Sava, 2015). Elastic extrapolation is feasible with multicomponent data recordings, and delivers more realistic reflectivity and valuable subsurface information, such as fracture distribution (Schoenberg, 1983; Grechka and Kachanov, 2006; Zhang et al., 2017). However, multiparameter inversion is subject to leakage (i.e., crosstalk) among inverted parameters (Operto et al., 2013; Pan and Innanen, 2016). Coupling between the multiple elastic wave modes (which become three in the presence of anisotropy) and their different illumination responses are responsible for such crosstalk, and leads to contamination of the inverted earth model. Considering the multitude of elastic modeling parameters and the reasons for choosing a certain parameterization, radiation pattern analysis is important to understand the ambiguity among physical properties with respect to the reflection angle and model parameterizations (Burridge et al., 1998; Köhn et al., 2012; Kamath and Tsvankin, 2016; Oh and Alkhalifah, 2016). This analysis also shows that the amplitude responses overlap for different earth model contrasts, thus expressing the difficulty to isolate sensitivity kernels for different parameters. In addition, limited acquisition coverage and subsurface complexity contributes to highly irregular illumination, thus reducing the effectiveness of radiation pattern analysis.

To mitigate the crosstalk between inverted elastic model parameters and, therefore, obtain a more geological-plausible earth model, various authors propose to use known physical relationships between parameters to constrain the elastic inversion. Baumstein (2013) imposes box constraints (i.e., allowed maximum and minimum values for a certain model parameter) using projection onto convex sets, while Peters et al. (2015) apply a similar method with additional smoothness constraints. Instead of simply imposing box constraints, Duan and Sava (2016) perform data-domain wavefield tomography using logarithmic barrier constraints based on known linear petrophysical relationships between P- and S-wave velocities. Such barrier constraints are incorporated in the inversion by an additional term in the objection function, as opposed to constraints imposed at the line search step with convex sets formulation. This methodology delivers more realistic earth models since crosstalk and artifacts do not obey petrophysical properties and are attenuated during inversion with imposition of such constraints.

Inter-parameter crosstalk represents one of the main challenges facing elastic wavefield tomography, as we seek an earth model that matches the data and also generates high-quality images. Our choice is to impose physical constraints on the earth model and implement a scheme that simultaneously optimizes the model and the migrated image. Therefore, we impose logarithmic barrier constraints similarly to the method by Duan and Sava (2016), but applied in the context of mixed-domain elastic wavefield tomography, i.e., elastic RWI. Therefore, our method avoids the combined harmful effect of inter-parameter crosstalk (by physical constraints) and high-wavenumber updates (by low-wavenumber RWI gradients) into the inversion. The total model is constructed by adding the smooth background and the sharp perturbation models. However, such sharp contrasts cause backscattering during wavefield extrapolation, thus producing low-wavenumber artifacts when implementing conventional imaging conditions, including the ones based on model perturbations. We address this problem by applying the energy imaging condition in a least-squares sense (Rocha et al., 2016, 2017; Rocha and Sava, 2018) for imaging with the total earth model.

2 THEORY

Reflection waveform inversion involves decomposition of the extrapolated wavefields into their background and scattered constituents, as well as separation of the earth model into smooth and rough components. We obtain the rough models through least-squares migration based on the separated background and scattered wavefields. For updating the smooth earth model, we use wavefield tomography also based on this single-scattering wavefield decomposition. We incorporate a physical constraint term in the objective function of wavefield

tomography, thus leading the inversion toward plausible models that satisfy known petrophysical relationships.

2.1 Single-scattering and migration operators based on earth model perturbations

We consider the second-order elastic wave equation for isotropic media

$$\rho\ddot{\mathbf{u}} - \nabla\left[\lambda\left(\nabla\cdot\mathbf{u}\right)\right] - \nabla\cdot\left[\mu\left(\nabla\mathbf{u}+\nabla\mathbf{u}^{\mathrm{T}}\right)\right] = \mathbf{f}\ , \quad (1)$$

where $\mathbf{u}\left(\mathbf{x},t\right)$ is the wavefield, $\mathbf{f}\left(\mathbf{x},t\right)$ is the source term, $\lambda\left(\mathbf{x}\right)$ and $\mu\left(\mathbf{x}\right)$ are Lamé parameters, $\rho\left(\mathbf{x}\right)$ is the density of the medium, ∇ represents spatial derivative operators, and the superscript dot indicates time differentiation. Under the single-scattering assumption, one can consider each one of the medium parameters as composed of a background and a small perturbation. Similarly, the associated wavefield is also decomposed into background and weak-scattering parts. Therefore, we can write

$$\rho = \rho_0 + \delta\rho\ , \quad (2)$$

$$\lambda = \lambda_0 + \delta\lambda\ , \quad (3)$$

$$\mu = \mu_0 + \delta\mu\ , \quad (4)$$

$$\mathbf{u} = \mathbf{u}_0 + \delta\mathbf{u}\ , \quad (5)$$

where δ indicates small perturbations, and the subscript $_0$ indicates background quantities. Substituting equations 2-5 in equation 1, and ignoring higher-order terms involving the product of the small earth model perturbations with $\delta\mathbf{u}$, we obtain

$$\begin{aligned}\rho_0\ddot{\delta\mathbf{u}} - \nabla\left[\lambda_0\left(\nabla\cdot\delta\mathbf{u}\right)\right] - \nabla\cdot\left[\mu_0\left(\nabla\delta\mathbf{u}+\nabla\delta\mathbf{u}^{\mathrm{T}}\right)\right] = \\ -\delta\rho\ddot{\mathbf{u}}_0 + \nabla\left[\delta\lambda\left(\nabla\cdot\mathbf{u}_0\right)\right] + \nabla\cdot\left[\delta\mu\left(\nabla\mathbf{u}_0+\nabla\mathbf{u}_0^{\mathrm{T}}\right)\right] + \mathbf{f}\ .\end{aligned} \quad (6)$$

We write equation 6 to indicate the interaction between model perturbations $(\delta\rho,\delta\lambda,\delta\mu)$ and the background wavefield $\mathbf{u}_0$ is in the source term for the scattered wavefield $\delta\mathbf{u}$, which captured at receiver locations $\mathbf{x}_r$ leads to the scattered data $\delta\mathbf{d}\left(\mathbf{x}_r,t\right) = \mathbf{K}_r\delta\mathbf{u}$ ($\mathbf{K}_r$ is an operator that extracts $\delta\mathbf{u}$ at $\mathbf{x}_r$ forming $\delta\mathbf{d}$). Therefore, we can write the model perturbations generating recorded scattered data as

$$\delta\mathbf{d} = \mathbf{K}_r\delta\mathbf{u} = \mathbf{L}\delta\mathbf{m}\ , \quad (7)$$

where $\delta\mathbf{m} = \left[\delta\rho\ \ \delta\lambda\ \ \delta\mu\right]^{\mathrm{T}}$, and $\mathbf{L}$ is the single-scattering operator (see Appendix A). Its adjoint is the migration operator

$$\delta\mathbf{m}_{mig} = \mathbf{L}^{\mathrm{T}}\delta\mathbf{d}\ . \quad (8)$$

For more than one experiment (e.g., shot gather), $\delta\mathbf{d}$ also depends on the experiment index e. In this case, $\mathbf{L}^{\mathrm{T}}$ involves summation over migrated images from different experiments, and $\mathbf{L}$ sprays $\delta\mathbf{m}$ for different modelings.

Least-squares migration leads to a more robust perturbation image by minimizing the following objective function

$$\mathcal{J}_{LSM} = \frac{1}{2}\|\mathbf{L}\delta\mathbf{m} - \delta\mathbf{d}\|^2\ , \quad (9)$$

where the subscript LSM stands for least-squares migration. Using equations 7 and 8, the image that minimizes equation 9 in a least-squares sense corresponds to

$$\delta\mathbf{m}_{LS} = \left(\mathbf{L}^{\mathrm{T}}\mathbf{L}\right)^{-1}\mathbf{L}^{\mathrm{T}}\delta\mathbf{d}\ . \quad (10)$$

Equation 10 describes a procedure that only inverts for the model perturbation $\delta\mathbf{m}$, while keeping the background model $\mathbf{m}_0 = \left[\rho_0\ \ \lambda_0\ \ \mu_0\right]^{\mathrm{T}}$ unchanged. In order to update the background model, we need to perform non-linear inversion with updates computed by the adjoint-state method. Instead of simply applying the migration operator, inverting for $\delta\mathbf{m}$ helps the subsequent inversion for $\mathbf{m}_0$ by providing a higher-quality image with fewer artifacts for more accurate single-scattering modeling.

2.2 Waveform inversion with background and scattered wavefields

Equation 1 can also be formulated as

$$\mathbf{A}(\mathbf{m})\mathbf{u} = \mathbf{f}\ , \quad (11)$$

where $\mathbf{A}(\mathbf{m})$ is the elastic wave-equation operator, which is non-linear and depends on the total model vector $\mathbf{m} = \left[\rho\ \ \lambda\ \ \mu\right]^{\mathrm{T}}$. The total wavefield computed by equation 11 is captured at receiver locations (again, by the extraction operator $\mathbf{K}_r$) and forms the modeled data $\mathbf{d}\left(\mathbf{x}_r,t\right)$, which is then compared with observed data in waveform inversion by the following objective function

$$\mathcal{J}_D = \sum_e \frac{1}{2}\|\mathbf{d} - \mathbf{d}_{obs}\|^2 = \sum_e \frac{1}{2}\|\mathbf{K}_r\mathbf{u} - \mathbf{d}_{obs}\|^2\ , \quad (12)$$

where the summation over experiments (e.g., shot gathers) is indicated by the index e, and the subscript D indicates that the objective function involves only data comparison. In order to construct the model update in waveform inversion, one needs to compute the gradient of the objective function in equation 12 with respect to the model parameters. Based on adjoint-state theory (Tarantola, 1988; Plessix, 2006; Sava, 2014), such gradient is represented by

$$\frac{\partial\mathcal{J}_D}{\partial\mathbf{m}} = \sum_e \frac{\partial\mathbf{A}}{\partial\mathbf{m}}\mathbf{u}\star\mathbf{a}\ . \quad (13)$$

The derivative of the wave-equation operator with respect to model parameters ($\frac{\partial\mathbf{A}}{\partial\mathbf{m}}$) is detailed in Appendix B. The symbol $\star$ in equation 13 represents zero-lag crosscorrelation between the state ($\mathbf{u}$) and adjoint ($\mathbf{a}$) wavefields. The adjoint wavefield uses the adjoint wave-equation operator and the objective function derivative with respect to the state wavefield as its source term:

$$\mathbf{A}^{\mathrm{T}}(\mathbf{m})\mathbf{a} = \frac{\partial\mathcal{J}_D}{\partial\mathbf{u}} = \mathbf{K}_r^{\mathrm{T}}\left(\mathbf{d} - \mathbf{d}_{obs}\right)\ . \quad (14)$$

Conventional full-waveform inversion uses the gradient expression in equation 13. However, for reflection-waveform inversion, both state and adjoint wavefields are decomposed into background and scattered parts based on equation 5. Such wavefield decomposition uses the single-scattering modeling expressed in equation 6, and thus the model perturbation vec-

tor $\delta\mathbf{m}$. We rewrite equation 13 as

$$\frac{\partial \mathcal{J}_D}{\partial \mathbf{m}} = \sum_e \frac{\partial \mathbf{A}}{\partial \mathbf{m}} \left(\mathbf{u}_0 + \delta\mathbf{u}\right) \star \left(\mathbf{a}_0 + \delta\mathbf{a}\right) \ . \tag{15}$$

Distributing the zero-lag cross correlation in equation 15, we obtain four terms for the total gradient:

$$\begin{aligned} \frac{\partial \mathcal{J}_D}{\partial \mathbf{m}} &= \sum_e \frac{\partial \mathbf{A}}{\partial \mathbf{m}} \mathbf{u}_0 \star \delta\mathbf{a} + \sum_e \frac{\partial \mathbf{A}}{\partial \mathbf{m}} \delta\mathbf{u} \star \mathbf{a}_0 \\ &+ \sum_e \frac{\partial \mathbf{A}}{\partial \mathbf{m}} \mathbf{u}_0 \star \mathbf{a}_0 + \sum_e \frac{\partial \mathbf{A}}{\partial \mathbf{m}} \delta\mathbf{u} \star \delta\mathbf{a} \ . \end{aligned} \tag{16}$$

The separation between background and scattered wavefields is useful to obtain the low-wavenumber content of the waveform inversion gradient. The first summation in equation 16 involves crosscorrelation of waves propagating from the source to the image point, while the second summation correlates waves propagating from the receivers to the image point. Hence, such events coincide in space and time along their similar propagation paths, resulting in low-wavenumber content. The other two terms involve crosscorrelation of waves that only coincide at the image point, producing reflectivity that is characterized by high wavenumbers. In that sense, the low-wavenumber gradient corresponds to the background model ($\mathbf{m}_0$) update. Therefore, the RWI gradient is

$$\frac{\partial \mathcal{J}_D}{\partial \mathbf{m}_0} = \sum_e \left[\frac{\partial \mathbf{A}}{\partial \mathbf{m}} \mathbf{u}_0 \star \delta\mathbf{a} + \frac{\partial \mathbf{A}}{\partial \mathbf{m}} \delta\mathbf{u} \star \mathbf{a}_0 \right] \ . \tag{17}$$

2.3 Physical constraints

Auxiliary terms in the objective function that act in the model space are useful to prevent inversion results with unphysical models, which commonly emerge with data-misfit objection functions. The most familiar model objective function term penalizes inverted models far from a known reference model:

$$\mathcal{J}_M = \frac{1}{2} \mathbf{W}_m \|\mathbf{m} - \mathbf{m}_{\text{ref}}\|^2 \ , \tag{18}$$

where $\mathbf{W}_m$ is called model weighting matrix, and subscript "ref" stands for reference model. Such matrix can be a shaping operator, or more simply, a diagonal operator imposing larger weights on certain parts of the model space. For instance, considering updates in λ and μ while keeping density ρ constant, the gradient of equation 18 with respect to model parameters is

$$\frac{\partial \mathcal{J}_M}{\partial \lambda} = \mathbf{W}_\lambda^{\mathrm{T}} \mathbf{W}_\lambda \left(\lambda - \lambda_{\text{ref}}\right) \ , \tag{19}$$

$$\frac{\partial \mathcal{J}_M}{\partial \mu} = \mathbf{W}_\mu^{\mathrm{T}} \mathbf{W}_\mu \left(\mu - \mu_{\text{ref}}\right) \ . \tag{20}$$

An additional model objective function term exploits known physical relationships between two sets of model parameters, for example, implemented by a logarithmic penalty function (Peng et al., 2002; Gasso et al., 2009; Duan and Sava, 2016):

$$\mathcal{J}_C = -\eta \sum_{\mathbf{x}} \left[\log(h_u) + \log(h_l)\right] \ , \tag{21}$$

where η is a weighting scalar parameter relative to the other objective function terms, while h_u and h_l define linear functions in the dual-model space determining its upper and lower bounds. Note that equation 21 involves summation over all model samples. If we want to constrain the model parameters λ and μ, we write the upper and lower bounds as

$$h_u = -\lambda + c_u \mu + b_u = 0 \ , \tag{22}$$

$$h_l = \lambda - c_l \mu - b_l = 0 \ , \tag{23}$$

where $c_{u,l}$ and $b_{u,l}$ are the slopes and intercepts of the lines. For model pairs that fall inside the region bounded by h_u and h_l, the distance to the barrier lines determines the value of the physical constraint. On one hand, the further and more equidistant to h_u and h_l a certain model sample is, the larger is the argument of the logarithm, and therefore, smaller is $\mathcal{J}_C$. On the other hand, model samples that are close to one of the barrier lines during inversion lead to large $\mathcal{J}_C$, and are thus forced to move away from that barrier.

The gradient of equation 21 with respect to either λ or μ is

$$\frac{\partial \mathcal{J}_C}{\partial \lambda} = \frac{-\eta}{\lambda - c_u \mu - bu} - \frac{\eta}{\lambda - c_l \mu - bl} \ , \tag{24}$$

$$\frac{\partial \mathcal{J}_C}{\partial \mu} = \frac{\eta c_u}{\lambda - c_u \mu - bu} + \frac{\eta c_l}{\lambda - c_l \mu - bl} \ . \tag{25}$$

Equations 24 and 25 show that the gradient tends to ∞ if any of its denominators tends to zero. This happens for model samples that get close to one of the barriers. Therefore, the physical constraint term ensures that the inverted models are between these bounds by imposing large corrective updates to anomalous model samples relative to the desired petrophysical trend.

Finally, we can write the total objective function involving data-misfit term, model-misfit tern with respect to a reference model, and petrophysical constraint term:

$$\mathcal{J} = \mathcal{J}_D + \mathcal{J}_M + \mathcal{J}_C \ . \tag{26}$$

3 EXAMPLES

The following numerical examples demonstrate how imposing model regularization and petrophysical constraints delivers more geological-plausible ERWI models. We also obtain improved convergence rates and image quality when compared to unconstrained inversion. We apply the method on a simple experiment with a single reflector and a Gaussian anomaly. We also illustrate the method with a more complex and realistic synthetic model. In all cases, we assume that petrophysical information is available to constrain the model parameters.

3.1 Single-reflector with a Gaussian anomaly

We illustrate our ERWI method with the synthetic elastic model shown in Figure 1, where the top of Figures 1(a) and 1(b) show the acquisition geometry, the reflector location and the Gaussian anomalies for the true λ and μ models, respectively. We start inversion from a constant background; and

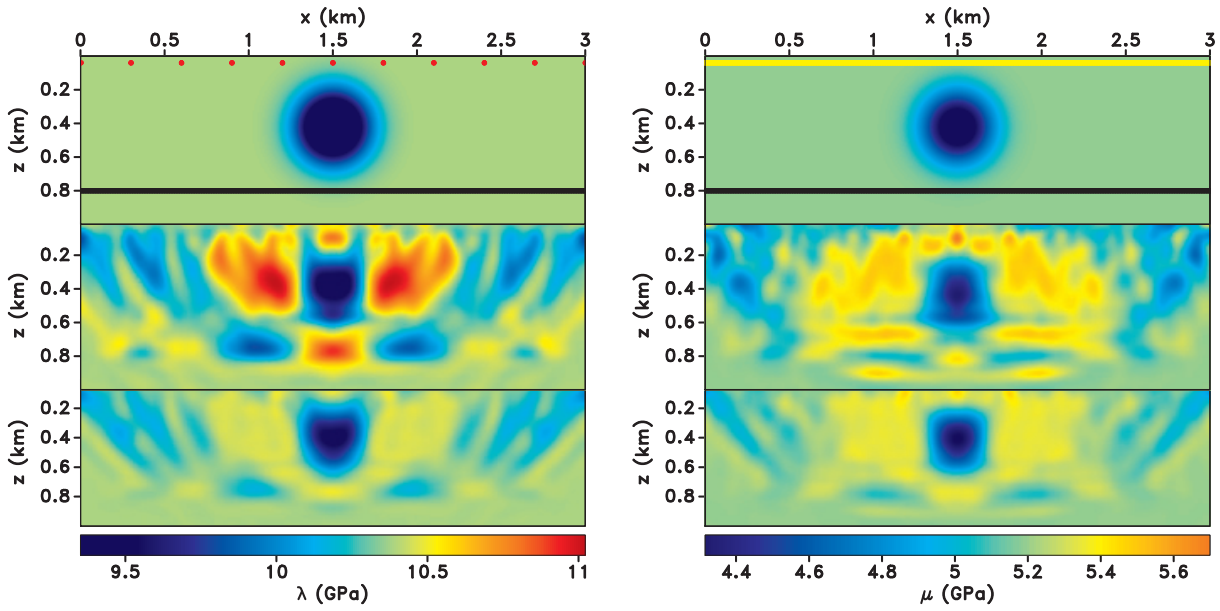


Figure 1. True (top), unconstrained (middle), and constrained (bottom) inverted models for (a) λ and (b) μ. The top panels also show the 11 sources (red) and the line of multicomponent receivers (yellow), and the reflector (black). Adding the physical constraint term into the inversion mitigates the spurious artifacts from inter-parameter crosstalk and sparse acquisition, delivering a more plausible earth model.

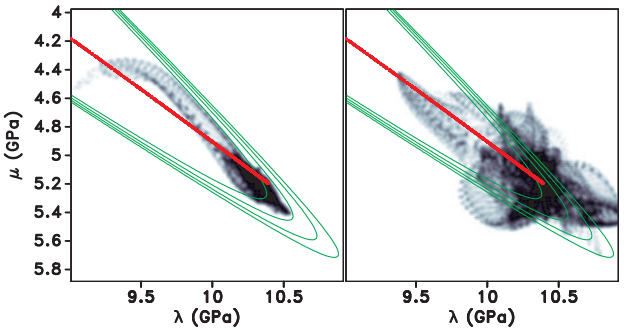


Figure 2. Crossplot in λ-μ space of inverted models: unconstrained (left) and constrained (right). The red line corresponds to the true model. The logarithmic barrier function used in the constrained inversion is plotted with the green contour lines. The unconstrained inverted model is spread throughout the model space without following a trend, while the constrained model is restricted to the region delimited by the barrier.

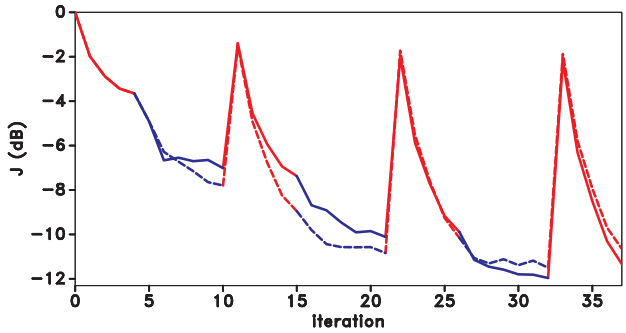


Figure 3. Objective functions in decibel scale for unconstrained (dashed) and constrained (solid) ERWIs, which alternate between least-squares migration of model perturbations (red) and waveform inversion of background model (blue). Note how constrained ERWI performs better at the final iterations for both smooth model (at iteration 32) and image (final) inversions.

after 38 inversion iterations, alternating between smooth and rough model updates, we obtain the unconstrained (middle of Figure 1) and constrained (bottom of Figure 1) models. Note how the constrained ERWI mitigates the spurious artifacts (around the anomaly) existent in the unconstrained inverted model, which are caused by a combination of sparse geometry, limited bandwidth and crosstalk between model parameters.

The constraint term uses two barrier lines defined by $h_l = \lambda - 1.5\mu - 1.98$ and $h_u = -\lambda + \mu + 5.43$ according to equations 22 and 23. Figure 2 shows all model samples from unconstrained and constrained inversions. The green contour lines in Figure 2 indicate constant values of $\mathcal{J}_C$ and exhibit two visible convergent barrier lines. The unconstrained model samples are more broadly spread into the model space, while the constrained samples are confined within the barriers and closer to the line of true model samples. The point at $[\mu, \lambda] = [5.194, 10.388]$ GPa represents the background model value, from where both constrained and unconstrained inversions start. Both unconstrained and constrained ERWIs alternate between image (rough model) and background (smooth model)

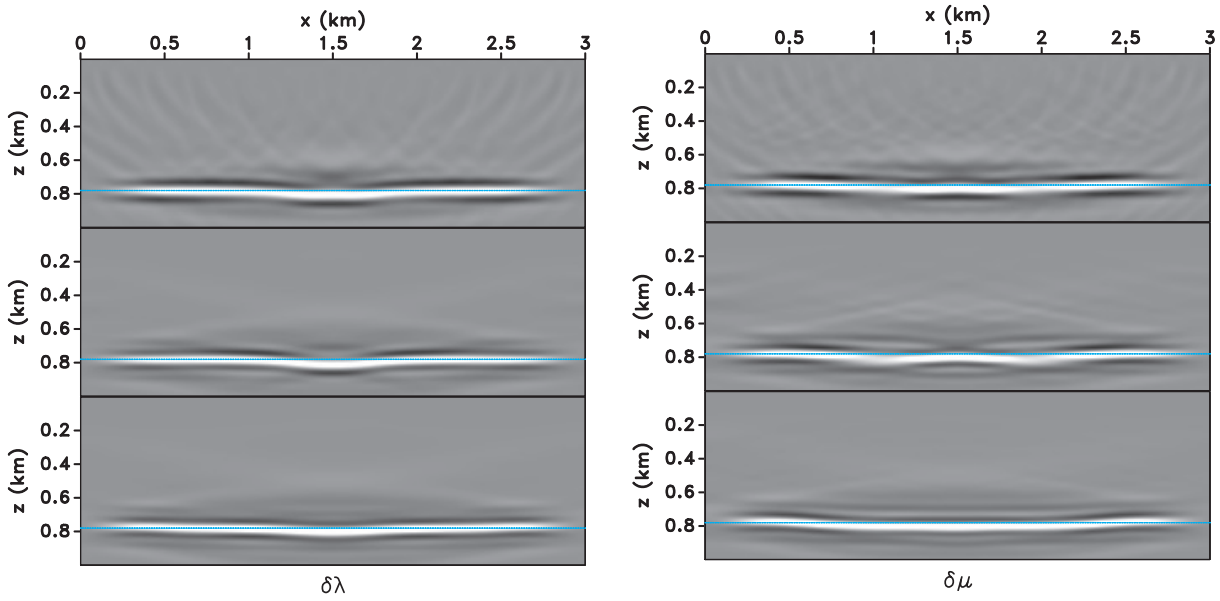


Figure 4. RTM (top) and LSRTM (middle) images obtained with the initial velocity, and LSRTM (bottom) images obtained with constrained inverted velocities for (a) $\delta\lambda$ and (b) $\delta\mu$. The faint dashed cyan line corresponds to the true reflector. Note the sparse acquisition artifacts in RTM, the irregularity of the imaged flat reflector for RTM and LSRTM as imprint of wrong velocity, and the improved reflector flatness and focusing for LSRTM with the constrained inverted velocity.

inversions as shown in the objective function plot in Figure 3. The unconstrained inversion has a smaller objective function for the first 20 iterations. However, for the remaining iterations, the constrained ERWI has better performance, finalizing with smaller residuals for both smooth and rough model inversions relatively to the unconstrained ERWI.

To show how ERWI with physical constraints delivers a model that effectively increases image quality, we show the model perturbation $\delta\lambda$ and $\delta\mu$ images in Figures 4(a) and 4(b), respectively. The top reverse time migration (RTM) images show the cross-cutting artifacts due to sparse acquisition and a false subsidence of the flat reflector due to imaging with the wrong velocity (which is the initial velocity with the constant background value). Least-squares migration (LSRTM) on the same wrong model improves the image (middle of Figure 4) by mitigating the cross-cutting artifacts and sharpening the imaged reflector, but still exhibits the imprint of the wrong velocity at the center of the reflector for $\delta\lambda$, and at $[x, z] = [1, 0.8]$ km and $[x, z] = [2, 0.8]$ km for $\delta\mu$. Finally, using the constrained ERWI model, LSRTM delivers the bottom images in Figure 4, which show a horizontal reflector closer to the true one.

3.2 Marmousi II

We test our method on a portion of the Marmousi II model (Martin et al., 2002) with independent P- and S-wave velocities. The model parameters, acquisition geometry and well locations used in our experiment are shown in Figure 5. Figure 5(a) shows the λ model, the horizontal line of receivers that record the displacement field at every grid point of the water bottom ($z = 0.17$ km), the 17 pressure sources located near the surface of the water layer ($z = 0.05$ km) spaced by 0.250 km. This acquisition geometry resembles a multicomponent ocean bottom seismic survey (OBS). Figure 5(b) shows the μ model and the three well locations at $x = [0.5, 2.1, 3.7]$ km, from where we have an estimate of the true model parameters, as shown in Figure 6. In the following ERWI experiments, we use a 7.5 Hz peak Ricker wavelet for the source signature.

Figure 7 shows the initial model (top), the reference model (middle) used in the definition of $\mathcal{J}_M$ (equation 18), and a low-pass version of the true model (bottom) that corresponds to the maximum resolution possible with the source wavelet of 7.5 Hz. We apply image-guided interpolation (Hale, 2009, 2010) to construct the reference model using as input the LSRTM energy image (Rocha et al., 2016, 2017; Rocha and Sava, 2018) computed with the initial velocity (second image from top to bottom in Figure 11(b)), and the three velocity profiles from the well locations (Figure 6).

Figure 8 shows the inverted models for data-misfit minimization only ($\mathcal{J}_D$, top), data-misfit term plus reference model term ($\mathcal{J}_D + \mathcal{J}_M$, middle), and all three objection function terms including the petrophysical constraint ($\mathcal{J}_D + \mathcal{J}_M + \mathcal{J}_C$, bottom). Note the spurious artifacts that contaminate the model in the $\mathcal{J}_D$ inversion, and how they are attenuated with the introduction of the $\mathcal{J}_M$ and $\mathcal{J}_C$ terms. Comparing middle and bottom models in Figure 8, we note that adding only $\mathcal{J}_M$ is not sufficient for attenuating most of these artifacts, and

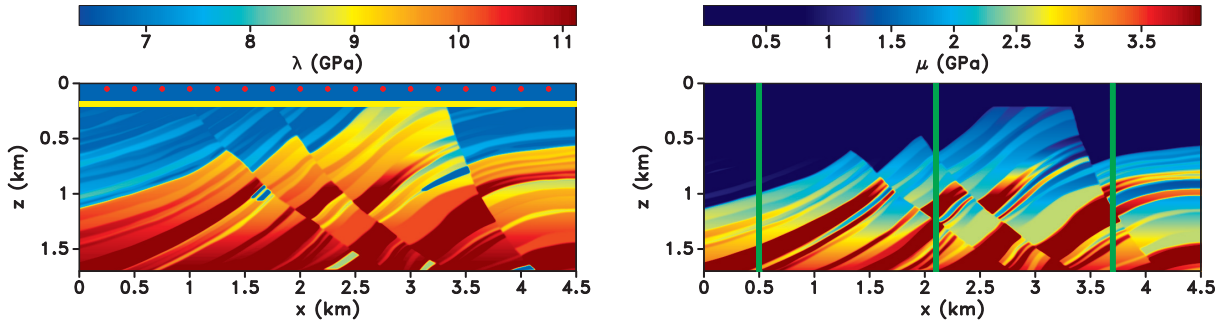


Figure 5. Lamé parameters λ (a) and μ (b) from the Marmousi II model. The acquisition geometry, which consists of 17 pressure sources (red) near the water surface and a line (yellow) of multicomponent receivers, is also shown in (a). The locations for the three wells used as prior information are indicated by green lines in (b).

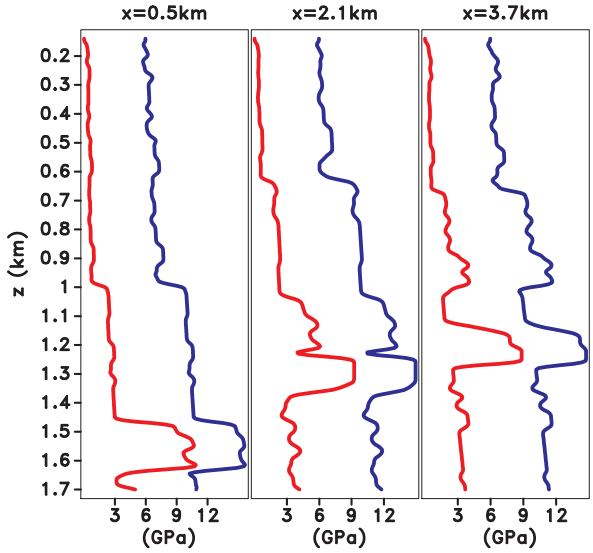


Figure 6. Lamé parameters λ (blue) and μ (red) well-log profiles at the three locations shown in Figure 5. This information is used for the reference model ($\mathcal{J}_M$) and to define the petrophysical constraints ($\mathcal{J}_C$) implemented in the ERWI experiments.

therefore, the ERWI involving all three terms leads to the best inverted model.

To show how petrophysical constraints force the inverted model to follow the estimated geological trend from the wells, we show $\lambda-\mu$ plots in Figure 9. We only apply the petrophysical constraints to the shallow model part (with values ranging from $[\lambda,\mu] = [5.75, 0]$ GPa to $[\lambda,\mu] = [7.5, 1.1]$ GPa) since it delivers the greatest impact in image quality. In addition, deeper model formations obey different $\lambda-\mu$ ratios, requiring the implementation of multiple constraint terms, which we avoid in these experiments for simplicity. Each individual plot in Figure 9 shows contour lines representing constant values of $\mathcal{J}_C$ in the selected model space. Figure 9(a) shows the model points from the three well locations, which serve as the basis for the constraint barriers $h_l = \lambda - 3.1\mu - 4.0$ and $h_u = -\lambda + 3.1\mu + 6.0$. Figure 9(b) shows the model pairs for the unconstrained inversion (J_D only) and how they spread beyond the barrier lines. Figure 9(c) shows the model samples for the constrained inversion ($\mathcal{J}_D + \mathcal{J}_M + \mathcal{J}_C$), which follow the imposed trend. The constrained model samples are mostly concentrated in the midpoint between the two barriers, but some samples comply more with data, as indicated by the points concentrated in the bottom-left corner ($\mu > 0.5$ GPa and $\lambda > 7.3$ GPa). Also, by observing the true model cross-plot in Figure 9(d), we note that the constrained model in Figure 9(c) is closer to the true one relative to the unconstrained model in Figure 9(b).

Figure 10 shows the objective function evolution over iterations for both unconstrained (J_D) and constrained ($\mathcal{J}_D + \mathcal{J}_M + \mathcal{J}_C$) ERWIs. As explained previously, ERWI alternates between rough (red graph) and (blue) smooth model updates. Similarly to the simple reflector experiment, the unconstrained inversion exhibits better performance in the first iterations, up to iteration 17. For the remaining iterations, the constrained ERWI outperforms the unconstrained one, with smaller magnitude and less variation of its objective function.

To show the impact on image quality from wavefield tomography with petrophysical constraints, least-squares migration and energy imaging condition, we show a series of images in Figure 11. For higher resolution, we use a 15.0 Hz peak Ricker wavelet for all shown images as opposed to the source signature used to obtain the ERWI models. From top to bottom, Figures 11(a) (for $\delta\lambda$) and 11(b) (for energy imaging condition) show (1) RTM images with the initial velocity, (2) LSRTM images with the initial velocity, (3) LSRTM with the unconstrained ERWI model, (4) LSRTM with the constrained ERWI model, and (5) LSRTM with the true model. The energy images do not have backscattering artifacts characterized by low-wavenumber content, which otherwise occur for the perturbation images. Note the amplitude balance improvement, the mitigation of sparse-acquisition artifacts, and increase in reflectivity resolution from RTM (1) to LSRTM (2) even if imaging with incorrect velocity. Using the inverted velocities in (3) and (4) further improves LSRTM when compared to (2), with more obvious improvements in the $\delta\lambda$ im-

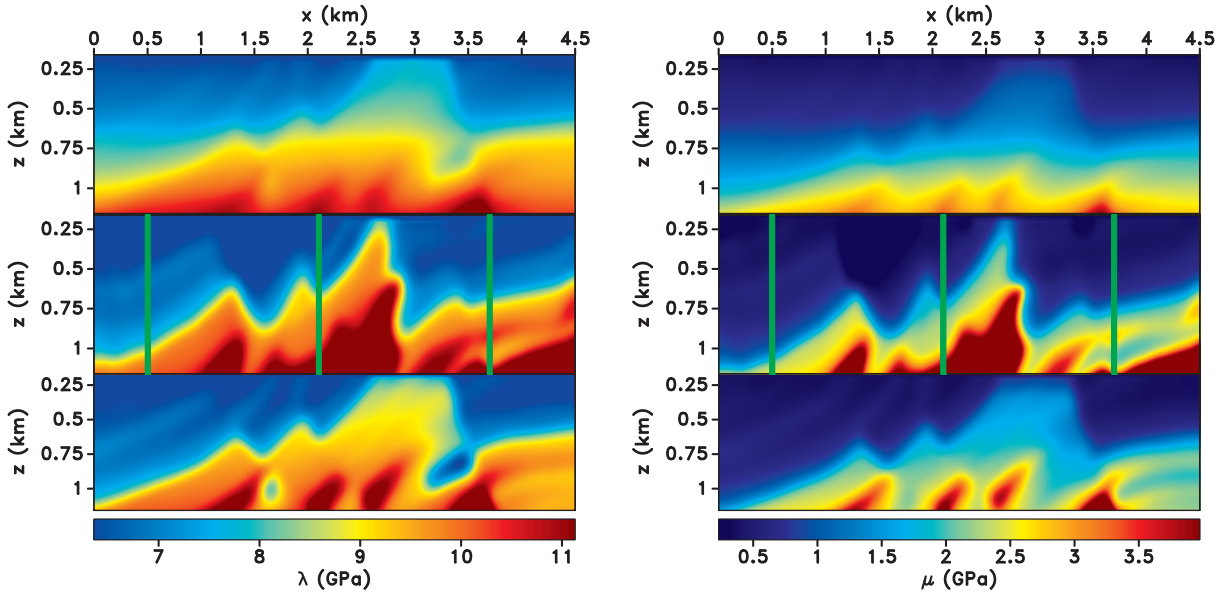


Figure 7. Initial (top), reference (middle) and low-pass true (bottom) models. The green lines indicate the three well locations used as input for the image-guided interpolation among wells to create the reference model.

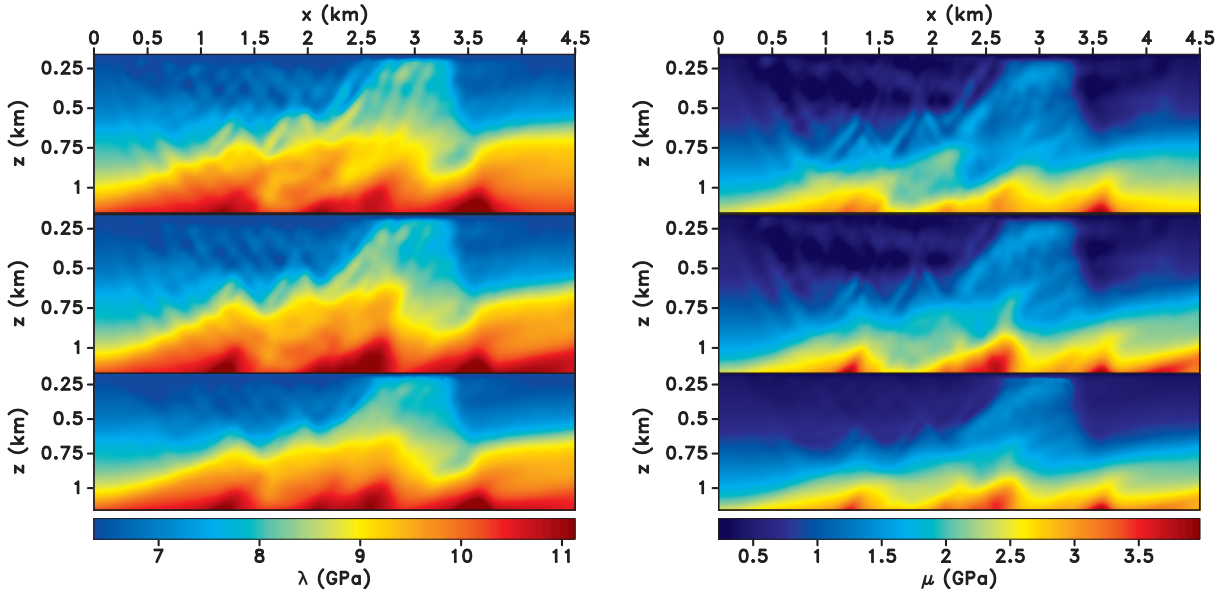


Figure 8. Inverted models using the objective functions $\mathcal{J}_D$ (top), $\mathcal{J}_D + \mathcal{J}_M$ (middle), and $\mathcal{J}_D + \mathcal{J}_M + \mathcal{J}_C$. Note the attenuation of spurious artifacts with addition of reference model term (middle), and further improvement with petrophysical constraint term (bottom).

ages around $[x, z] = [1.5, 0.4]$ km. The LSRTM images that use the constrained model (4) show slight improvements when compared to its unconstrained counterpart (3): the most obvious feature is the mitigation of four diffraction-like artifacts around $[x, z] = [1.0, 0.3]$ km in the energy images. For a complete comparison among all images, we show LSRTM images with the true velocity (5) which represent the optimal result.

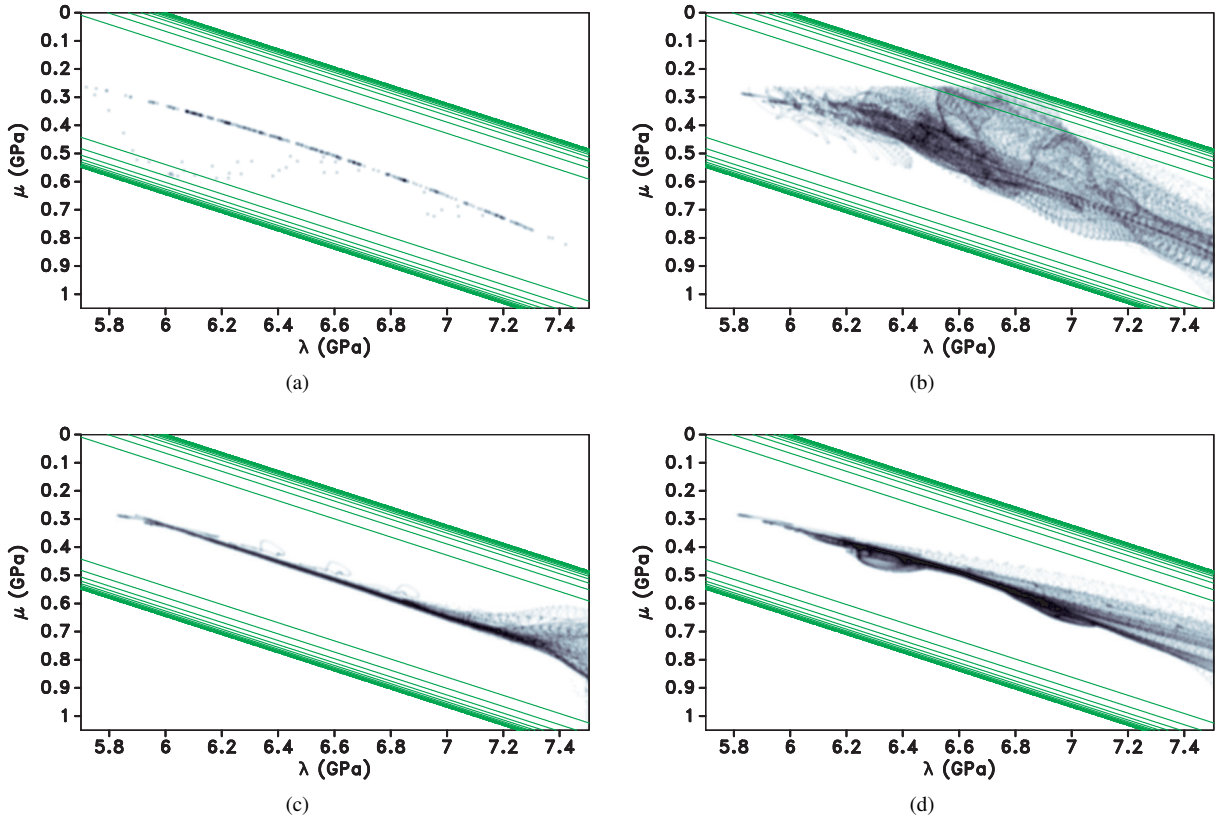


Figure 9. Crossplots in $\lambda - \mu$ space of (a) well-log samples, whose apparent slope is used to construct the barriers; (b) unconstrained inverted model; (c) constrained inverted model; and (d) true model. The green contour lines indicate constant values of $\mathcal{J}_C$. As opposed to the model points in (b), which do not follow a trend, the model pairs in (c) obey the imposed constrained constructed from (a) and conforms with the true model in (d).

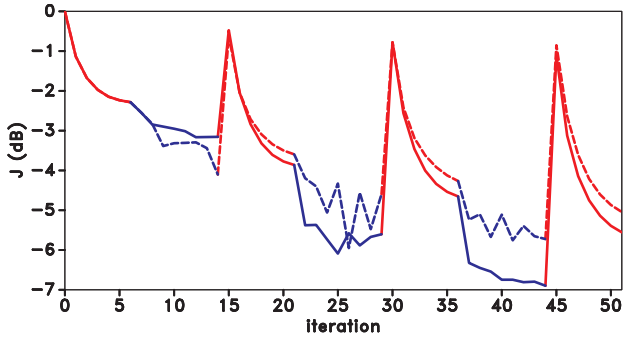


Figure 10. Objective functions in decibel scale for unconstrained (dashed) and constrained (solid) ERWIs, which alternate between least-squares migration of model perturbations (red) and waveform inversion of background model (blue). Note how constrained ERWI performs better at the final iterations for both the smooth model (at iteration 44) and the image (final) inversions. Also, the constrained ERWI objective function for waveform inversion (solid blue) exhibits less variation when compared to its unconstrained counterpart (dashed blue).

4 CONCLUSIONS

We use the mixed-domain elastic reflection waveform inversion framework, coupled with petrophysical constraints, to achieve both high-quality images and plausible earth models. Smooth updates are possible for the background model by separating the wavefields into their background and scattered constituents, whose proper correlation provides low-wavenumber gradients. Our model constraints are based on a linear trend derived from petrophysical input, which deters the inversion from delivering unphysical models with crosstalk artifacts. Although our constrained ERWI method has an additional constraint term in the objective function, we achieve improved convergence compared to conventional data-misfit minimization. We advocate for direct incorporation of prior geological information into wavefield tomography, which thus leads to robust model estimates and high-quality images, even with sparse acquisition and poor subsurface illumination.

5 ACKNOWLEDGMENTS

We thank the sponsors of the Center for Wave Phenomena (CWP), whose support made this research possible. We ac-

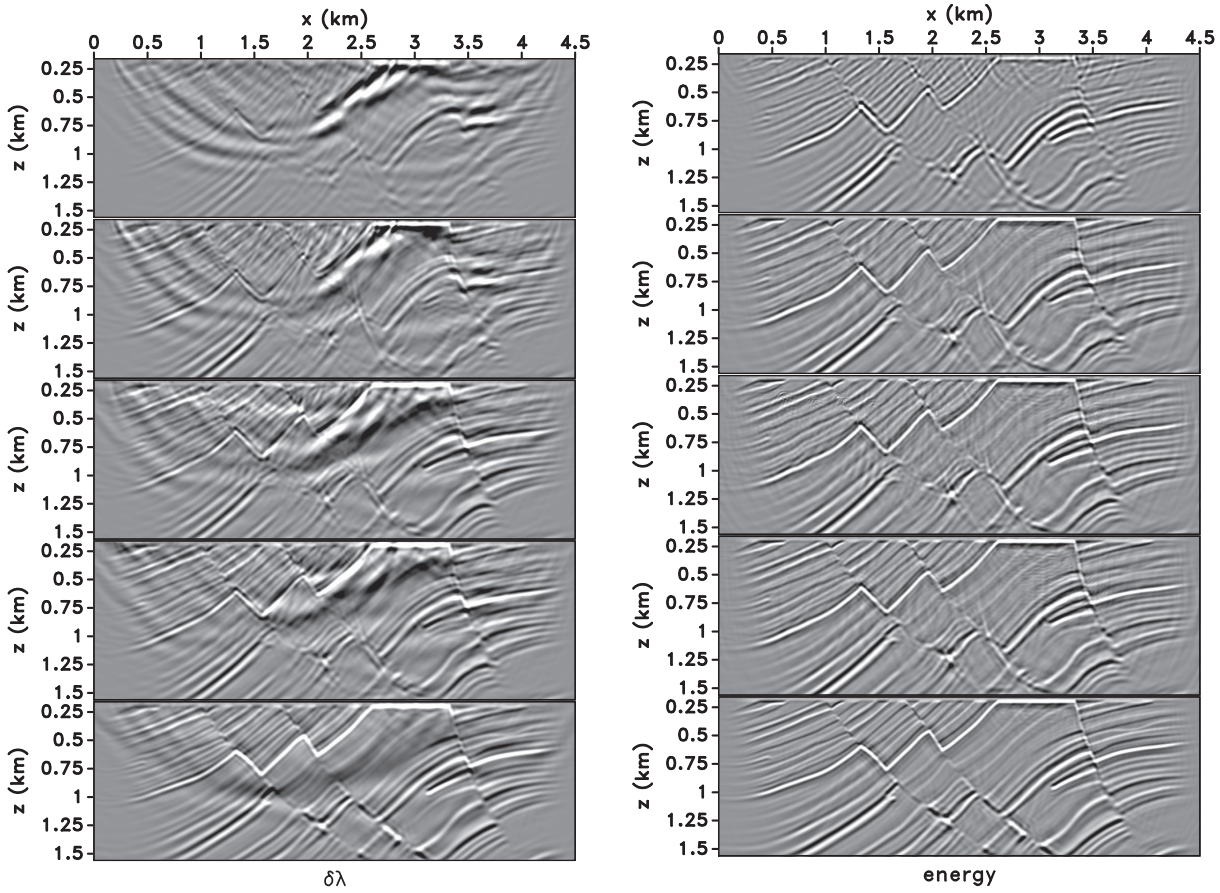


Figure 11. From top to bottom: (1) RTM images with the initial velocity, LSRTM images with (2) initial velocity, (3) unconstrained, (4) constrained and (5) true models, for $\delta\lambda$ (a) and energy (b) imaging conditions. Note how the energy images are higher-quality and do not show low-wavenumber artifacts. Also note how improving the velocity model leads to better focused reflectors, and how least-squares migration is superior to conventional migration.

knowledge Antoine Guitton and CWP iTeam members for helpful discussions. We are grateful to Vladimir Li for suggestions on the image-guided smoothing. The synthetic examples in this paper use the Madagascar open-source software package (Fomel et al., 2013) freely available from http://www.ahay.org.

REFERENCES

Albertin, U., P. Sava, J. Etgen, and M. Maharramov, 2005, Adjoint wave-equation velocity analysis: 76th Annual International Meeting, SEG, Expanded Abstracts, 3345–3349.

Alves, G., and B. Biondi, 2016, Imaging condition for elastic reverse time migration: 86th Annual International Meeting, SEG, Expanded Abstracts, 3959–3965.

Baumstein, A., 2013, POCS-based geophysical constraints in multiparameter full wavefield inversion: 75th European Association of Geoscientists and Engineers Conference and Exhibition.

Baysal, E., D. D. Kosloff, and J. W. C. Sherwood, 1983, Reverse time migration: Geophysics, **48**, 1514–1524.

Bishop, T., K. Bube, R. Cutler, R. Langan, P. Love, J. Resnick, R. Shuey, D. Spindler, and H. Wyld, 1985, Tomographic determination of velocity and depth in laterally varying media: Geophysics, **50**, 903–923.

Bording, R. P., A. Gersztenkorn, L. R. Lines, J. A. Scales, and S. Treitel, 1987, Applications of seismic traveltime tomography: Geophysical Journal of the Royal Astronomincal Society, **90**, 285–303.

Brossier, R., S. Operto, and J. Virieux, 2010, Which data residual norm for robust elastic frequency-domain full waveform inversion?: Geophysics, **75**, no. 3, R37–R46.

Burridge, R., M. V. de Hoop, D. Miller, and C. Spencer, 1998, Multiparameter inversion in anisotropic elastic media: Geophysical Journal International, **134**, 757–777.

Cerveny, V., 2005, Seismic ray theory: Cambridge University Press.

Chang, W.-F., and G. A. McMechan, 1987, Elastic reverse-

time migration: Geophysics, **52**, 1365–1375.

Chi, B., L. Dong, and Y. Liu, 2014, Full waveform inversion method using envelope objective function without low frequency data: Journal of Applied Geophysics, **109**, 36–46.

Diaz, E., P. Sava, and T. Yang, 2013, Data-domain and image-domain wavefield tomography: The Leading Edge, **32**, no. 1, 1064–1072.

Duan, Y., and P. Sava, 2015, Scalar imaging condition for elastic reverse time migration: Geophysics, **80**, no. 4, S127–S136.

———, 2016, Elastic wavefield tomography with physical model constraints: Geophysics, **81**, no. 6, R447–R456.

Duan, Y., P. Sava, and A. Guitton, 2017, Elastic least-squares reverse time migration: Geophysics, **82**, no. 4, S315–S325.

Feng, Z., and G. T. Schuster, 2017, Elastic least-squares reverse time migration: Geophysics, **82**, no. 2, S143–S157.

Fomel, S., P. Sava, I. Vlad, Y. Liu, and V. Bashkardin, 2013, Madagascar: open-source software project for multidimensional data analysis and reproducible computational experiments: Journal of Open Research Software, 8th ed., DOI: http://dx.doi.org/10.5334/jors.ag.

Gao, F., P. Williamson, and R. G. Pratt, 2014, A new objective function for full waveform inversion : differential semblance in the data domain: 84th Annual International Meeting, SEG, Expanded Abstracts, 1178–1183.

Gasso, G., A. Rakotomamonjy, and S. Canu, 2009, Recovering sparse signals with a certain family of non-convex penalties and DC programming: IEEE Transactions on Signal Processing, **57**, 4686–4698.

Gauthier, O., J. Virieux, and A. Tarantola, 1986, Two-dimensional nonlinear inversion of seismic waveforms: Numerical results: Geophysics, **51**, 1387–1403.

Grechka, V., and M. Kachanov, 2006, Effective elasticity of fractured rocks: A snapshot of the work in progress: Geophysics, **71**, no. 6, W45–W58.

Guo, Q., and T. Alkhalifah, 2017, Elastic reflection-based waveform inversion with a nonlinear approach: Geophysics, **82**, no. 6, R309–R321.

Hale, D., 2009, Imageguided blended neighbor interpolation of scattered data: 79th Annual International Meeting, SEG, Expanded Abstracts, 1127–1131.

———, 2010, Imageguided 3D interpolation of borehole data: 80th Annual International Meeting, SEG, Expanded Abstracts, 1266–1270.

Hicks, G. J., and R. G. Pratt, 2001, Reflection waveform inversion using local descent methods: estimating attenuation and velocity over a gas–sand deposit: Geophysics, **66**, no. 2, 598–612.

Hindlet, F., and P. Kolb, 1988, Inversion of prestack field data: An application to 1-D acoustic media: 58th Annual International Meeting, SEG, Expanded Abstracts, 1073–1076.

Hou, J., and W. W. Symes, 2018, Inversion velocity analysis in the subsurface-offset domain: Geophysics, **83**, R189–R200.

Kamath, N., and I. Tsvankin, 2016, Elastic full-waveform inversion for VTI media: methodology and sensitivity analysis: Geophysics, **81**, no. 2, C53–C68.

Köhn, D., D. D. Nil, A. Kurzmann, A. Przebindowska, and T. Bohlen, 2012, On the influence of model parameterization in elastic full waveform tomography: Geophysical Journal International, **191**, 325–345.

Lailly, P., 1983, The seismic inverse problem as a sequence of before stack migrations: Conference on Inverse Scattering, Theory and Application: Society of Industrial and Applied Mathematics, Expanded Abstracts, 206–220.

Lines, L. R., 1991, Applications of tomography to borehole and reflection seismology: The Leading Edge, **10**, no. 7, 11–17.

Ma, Y., and D. Hale, 2013, Wave-equation reflection traveltime inversion with dynamic warping and full-waveform inversion: Geophysics, **78**, no. 6, R223–R233.

Martin, G., K. Marfurt, and S. Larsen, 2002, Marmousi-2, an updated model for the investigation of avo in structurally complex areas: 72nd Annual International Meeting, SEG, Expanded Abstracts, 1979–1982.

McMechan, G. A., 1983, Migration by extrapolation of time dependent boundary values: Geophysical Prospecting, **31**, 413–420.

Mulder, W., and A. ten Kroode, 2002, Automatic velocity analysis by differential semblance optimization: Geophysics, **67**, 1184–1191.

Oh, J.-W., and T. Alkhalifah, 2016, Elastic orthorhombic anisotropic parameter inversion: an analysis of parameterization: Geophysics, **81**, no. 6, C279–293.

Operto, S., Y. Gholami, V. Prieux, A. Ribodetti, R. Brossier, L. Metivier, and J. Virieux, 2013, A guided tour of multiparameter full-waveform inversion with multicomponent data: from theory to practice: The Leading Edge, **32**, no. 9, 1040–1054.

Pan, W., and K. A. Innanen, 2016, A summary of several challenges facing multi-parameter elastic full waveform inversion: CSEG recorder, **41**, no. 8, 36–39.

Peng, J., C. Roos, and T. Terlaky, 2002, Self-regular functions and new search directions for linear and semidefinite optimization: Mathematical Programming, **93**, 129–171.

Peters, B., Z. Fang, B. R. Smithyman, and F. J. Herrmann, 2015, Regularizing waveform inversion by projections onto convex sets - application to the 2D Chevron 2014 synthetic blind-test dataset: University of British Columbia - Seismic Laboratory for Imaging and Modeling - Research Report.

Plessix, R. E., 2006, A review of the adjoint-state method for computing the gradient of a functional with geophysical applications: Geophysical Journal International, **167**, no. 2, 495–503.

Plessix, R. E., P. Milcik, H. Rynja, A. Stopin, K. Matson, and S. Abri, 2013, Multiparameter full-waveform inversion: Marine and land examples: The Leading Edge, **32**, no. 9, 1030–1038.

Ravasi, M., and A. Curtis, 2013, Elastic imaging with exact wavefield extrapolation for application to ocean-bottom 4C seismic data: Geophysics, **78**, no. 6, S265–S284.

Ren, Z., Y. Liu, and M. K. Sen, 2017, Least-squares reverse time migration in elastic media: Geophysical Journal International, **208**, no. 2, 1103–1125.

Rickett, J., and P. Sava, 2002, Offset and angle-domain common image-point gathers for shot-profile migration: Geophysics, **67**, 883–889.

Rocha, D., and P. Sava, 2018, Elastic least-squares reverse-time migration using the energy norm: Geophysics, **83**, no. 3, 000–000.

Rocha, D., N. Tanushev, and P. Sava, 2016, Isotropic elastic wavefield imaging using the energy norm: Geophysics, **81**, no. 4, S207–S219.

———, 2017, Anisotropic elastic wavefield imaging using the energy norm: Geophysics, **82**, no. 3, S225–S234.

Sava, P., 2014, A comparative review of wavefield tomography methods: Center for Wave Phenomena (CWP) Report # 802.

Sava, P., and B. Biondi, 2004a, Wave-equation migration velocity analysis - I: Theory: Geophysical Prospecting, **52**, 593–606.

———, 2004b, Wave-equation migration velocity analysis - II: Subsalt imaging example: Geophysical Prospecting, **52**, 607–623.

Sava, P., and I. Vasconcelos, 2011, Extended imaging condition for wave-equation migration: Geophysical Prospecting, **59**, 35–55.

Schoenberg, M., 1983, Reflection of elastic waves from periodically stratified media with interfacial slip: Geophysical Prospecting, **31**, 265–292.

Shen, P., and W. W. Symes, 2008, Automatic velocity analysis by shot profile migration: Geophysics, **73**, VE49–VE59.

Shen, P., W. W. Symes, and C. C. Stolk, 2005, *in* Differential semblance velocity analysis by waveequation migration.

Shin, C., and W. Ha, 2008, A comparison between the behavior of objective functions for waveform inversion in the frequency and Laplace domains: Geophysics, **73**, no. 5, VE119–VE133.

Sirgue, L., , and R. Pratt, 2004, Efficient waveform inversion and imaging: a strategy for selecting temporal frequencies: Geophysics, **69**, 231–248.

Symes, W., and J. Carazzone, 1991, Velocity inversion by differential semblance optimization: Geophysics, **56**, 654–663.

Symes, W. W., 2008, Migration velocity analysis and waveform inversion: Geophysical Prospecting, **56**, 765–790.

Tarantola, A., 1984, Inversion of seismic reflection data in the acoustic approximation: Geophysics, **49**, 1259–1266.

———, 1988, Theoretical background for the inversion of seismic waveforms including elasticity and attenuation: Pure and Applied Geophysics, **128**, 365–399.

Tromp, J., C. Tape, and Q. Liu, 2005, Seismic tomography, adjoint methods, time reversal and banana-doughnut kernels: Geophysical Journal International, **160**, 195–216.

Vigh, D., and W. Starr, 2008, 3D prestack plane-wave, full-waveform inversion: Geophysics, **73**, no. 5, VE135–VE144.

Virieux, J., and S. Operto, 2009, An overview of full-waveform inversion in exploration geophysics: Geophysics, **74**, no. 6, WCC1–WCC26.

Wang, S., F. Chen, H. Zhang, and Y. Shen, 2013, Reflection-based full-waveform inversion (RFWI) in the frequency domain: 83rd Annual International Meeting, SEG, Expanded Abstracts, 877–881.

Whitmore, N. D., 1983, Iterative depth migration by backward time propagation: 53rd Annual International Meeting, SEG, Expanded Abstracts, 382–385.

Xu, L., A. Stanton, and M. D. Sacchi, 2016, Elastic least squares reverse time migration: 86th Annual International Meeting, SEG, Expanded Abstracts, 3959–3965.

Xu, S., D. Wang, F. Chen, and Y. Zhang, 2012, Full waveform inversion for reflected seismic data: 74th European Association of Geoscientists and Engineers Conference and Exhibition.

Yan, J., and P. Sava, 2011, Improving the efficiency of elastic wave-mode separation for heterogeneous tti media: Geophysics, **76**, no. 4, T65–T78.

Yang, T., and P. Sava, 2011, Wave-equation migration velocity analysis with time-lag imaging: Geophysical Prospecting, **59**, 635–650.

———, 2015, Image-domain wavefield tomography with extended common-image-point gathers: Geophysical Prospecting, **63**, no. 1, 1086–1096.

Yang, Y., B. Engquist, J. Sun, and B. F. Hamfeldt, 2018, Application of optimal transport and the quadratic Wasserstein metric to full-waveform inversion: Geophysics, **83**, no. 1, R43–R62.

Zhang, Z., T. Alkhalifah, J.-W. Oh, and I. Tsvankin, 2017, Estimation of fracture parameters using elastic full-waveform inversion: 87th Annual International Meeting, SEG, Expanded Abstracts, 3272–3276.

Zhu, H., Y. Luo, T. Nissen-Meyer, C. Morency, and J. Tromp, 2009, Elastic imaging and time-lapse migration based on adjoint methods: Geophysics, **74**, WCA167–WCA177.

Appendix A

Single-scattering and migration operators based on model perturbations

We can write single-scattering modeling as

$$\delta\mathbf{d} = \mathbf{L}\delta\mathbf{m} = (\mathbf{K}_r\mathbf{A}\mathbf{S})\,\delta\mathbf{m}\;, \tag{A.1}$$

where

$$\mathbf{S} = \begin{bmatrix} -D_t\dot{u}_1^0 & D_1\left(u_{1,1}^0+u_{3,3}^0\right) & 2D_1u_{1,1}^0+D_3\left(u_{1,3}^0+u_{3,1}^0\right) \\ -D_t\dot{u}_3^0 & D_3\left(u_{1,1}^0+u_{3,3}^0\right) & 2D_3u_{3,3}^0+D_1\left(u_{1,3}^0+u_{3,1}^0\right) \end{bmatrix}, \tag{A.2}$$

$$\delta\mathbf{m} = \begin{bmatrix} \delta\rho \\ \delta\lambda \\ \delta\mu \end{bmatrix}\;, \tag{A.3}$$

and $\mathbf{A}$ is the elastic wave-equation extrapolator. Indices $i,j = \{1,3\}$ refer to $\{x,z\}$. $u_{i,j}^0$ is the j-th derivative of the ith-component of the background vector wavefield $\mathbf{u}^0$. The superscript dot on u_i^0 indicates time differentiation. D_t, D_1, and D_3 indicate derivative operators in time, x, and z, respectively, which are applied to the scattered wavefield instead of the background wavefield in the adjoint of single-scattering

modeling: migration,

$$\delta\mathbf{m} = \mathbf{L}^{\mathrm{T}}\delta\mathbf{d} = \left(\mathbf{S}^{\mathrm{T}}\mathbf{A}^{\mathrm{T}}\mathbf{K}_r^{\mathrm{T}}\right)\delta\mathbf{d}\ , \tag{A.4}$$

where

$$\mathbf{S}^{\mathrm{T}} = \begin{bmatrix} -\dot{u}_1^0 D_t & -\dot{u}_3^0 D_t \\ \left(u_{1,1}^0 + u_{3,3}^0\right) D_1 & \left(u_{1,1}^0 + u_{3,3}^0\right) D_3 \\ 2u_{1,1}^0 D_1 + \left(u_{1,3}^0 + u_{3,1}^0\right) D_3 & 2u_{3,3}^0 D_3 + \left(u_{1,3}^0 + u_{3,1}^0\right) D_1 \end{bmatrix}. \tag{A.5}$$

Most elastic LSRTM implementations use images based on model perturbations (Alves and Biondi, 2016; Feng and Schuster, 2017; Xu et al., 2016; Duan et al., 2017; Ren et al., 2017).

Appendix B

Waveform inversion gradients in isotropic elastic media based on adjoint-state method

The expression for the waveform inversion gradient in Equation 13 requires the computation of $\frac{\partial \mathbf{A}}{\partial \mathbf{m}}$, the derivative of the wave-equation operator with respect to model parameters (Tarantola, 1988; Tromp et al., 2005; Zhu et al., 2009). For each one of the model parameters, we have

$$\begin{bmatrix} \frac{\partial \mathbf{A}}{\partial \rho} \\ \frac{\partial \mathbf{A}}{\partial \lambda} \\ \frac{\partial \mathbf{A}}{\partial \mu} \end{bmatrix} \mathbf{u} = \begin{bmatrix} \frac{\partial}{\partial \rho} \\ \frac{\partial}{\partial \lambda} \\ \frac{\partial}{\partial \mu} \end{bmatrix} \left\{ \rho\ddot{\mathbf{u}} - \nabla\left[\lambda\left(\nabla\cdot\mathbf{u}\right)\right] - \nabla\cdot\left[\mu\left(\nabla\mathbf{u} + \nabla\mathbf{u}^{\mathrm{T}}\right)\right] - \mathbf{f} \right\}, \tag{B.1}$$

which leads to (using chain rule)

$$\begin{bmatrix} \frac{\partial \mathbf{A}}{\partial \rho} \\ \frac{\partial \mathbf{A}}{\partial \lambda} \\ \frac{\partial \mathbf{A}}{\partial \mu} \end{bmatrix} \mathbf{u} = \begin{bmatrix} \ddot{\mathbf{u}} \\ -\nabla\left(\nabla\cdot\mathbf{u}\right) \\ -\nabla\cdot\left(\nabla\mathbf{u} + \nabla\mathbf{u}^{\mathrm{T}}\right) \end{bmatrix}. \tag{B.2}$$

Therefore, we rewrite Equation 13 as

$$\frac{\partial \mathcal{J}_D}{\partial \mathbf{m}} = \begin{bmatrix} \frac{\partial \mathcal{J}_D}{\partial \rho} \\ \frac{\partial \mathcal{J}_D}{\partial \lambda} \\ \frac{\partial \mathcal{J}_D}{\partial \mu} \end{bmatrix} = \begin{bmatrix} \frac{\partial \mathbf{A}}{\partial \rho} \\ \frac{\partial \mathbf{A}}{\partial \lambda} \\ \frac{\partial \mathbf{A}}{\partial \mu} \end{bmatrix} \mathbf{u} \star \mathbf{a} = \begin{bmatrix} \ddot{\mathbf{u}} \star \mathbf{a} \\ -\nabla\left(\nabla\cdot\mathbf{u}\right) \star \mathbf{a} \\ -\nabla\cdot\left(\nabla\mathbf{u} + \nabla\mathbf{u}^{\mathrm{T}}\right) \star \mathbf{a} \end{bmatrix}. \tag{B.3}$$

Equation B.3 shows that the gradient expression for waveform inversion uses similar derivative operators involved in wavefield extrapolation.